CHEMISTRY OF MATERIALS
Article

Chem. Mater. **2009,** *21,* 4661–4668 4661
DOI:10.1021/cm901770n

Ionic Conductivity, Structure and Oxide Ion Migration Pathway in Fluorite-Based $Bi_8La_{10}O_{27}$

Yuandi Li,[†] Tom P. Hutchinson,[†] Xiaojun Kuang,[†] Peter R. Slater,[‡] Mark R. Johnson,[§] and Ivana Radosavljević Evans*[,†]

[†]*Department of Chemistry, Durham University, Science Site, Durham DH1 3LE, UK,* [‡]*School of Chemistry, University of Birmingham, Birmingham B15 2TT, UK, and* [§]*Institut Laue Langevin, F-38042 Grenoble, France*

Received June 24, 2009. Revised Manuscript Received August 24, 2009

The oxide ion conductor bismuth lanthanum oxide $Bi_8La_{10}O_{27}$ was studied by a combination of experimental and computational methods, including variable temperature X-ray and neutron diffraction, impedance spectroscopy, and ab initio molecular dynamics simulations. $Bi_8La_{10}O_{27}$ can be readily prepared by conventional solid state routes, and it crystallizes as a fluorite-related superstructure in space group *Immm*. It is stable up to 1000 °C, and it does not undergo any clear structural phase transition in this temperature region. $Bi_8La_{10}O_{27}$ exhibits oxide ion conductivity of $10^{-3}-10^{-2}$ S/cm between 600 °C and 1000 °C and a decrease of the activation energy from 0.869(8) eV below 600 °C to 0.722(3) eV above this temperature, presumably associated with increased mobility of oxide ions due to their local disordering. Ab initio molecular dynamics simulations provide a valuable insight into the conduction process in $Bi_8La_{10}O_{27}$ and identify the crystallographic sites involved in the conduction pathway.

Introduction

Oxide ion conductors are important functional materials with applications in oxygen sensors and pumps, membranes for oxygen separation, as well as electrolytes in solid oxide fuel cells.[1−4] One of the main factors which determines device operating temperature is the ionic conductivity of the solid electrolyte. Most current applications are based on the use of yttria stabilized zirconia (YSZ), which possesses excellent conducting properties but requires high operating temperatures (e.g., in solid oxide fuel cells, over 850 °C[5]). This is associated with numerous technical issues and increased costs, and there is a need to identify new materials which exhibit appreciable oxide ion conductivities at lower temperatures (500−750 °C[6]). A better understanding of chemical and structural factors that promote high oxide ion mobility and a deeper insight into conduction pathways and mechanisms is a key step in developing such materials.

The high temperature form of bismuth oxide, δ-Bi_2O_3, is one of the best oxide ion conductors known, but it is stable only between 730 °C and 824 °C.[7] The conducting properties of δ-Bi_2O_3 are associated with its structural features: the simultaneous presence of a highly polarizable cation network and an intrinsically disordered oxygen-deficient anion sublattice. It has been shown that the structure of δ-Bi_2O_3 can be stabilized to room temperature by partial substitution of Bi^{3+} by numerous cations, and this has led to the discovery of high oxide ion conductivity in a large number of materials.[8,9]

The title compound, $Bi_8La_{10}O_{27}$, was first prepared by Michel et al.[10] who described it as an oxygen-deficient δ-Bi_2O_3 based superstructure with unit cell parameters $a = 12.079(2)$ Å, $b = 16.348(4)$, and $c = 4.0988(5)$ Å and space group *Immm*. They used room temperature powder neutron diffraction data to obtain the final structural model which contained an oxygen atom site with partial fractional occupancy and a high isotropic temperature factor.

The existence of partially occupied crystallographic sites located along channels in a δ-Bi_2O_3 based superstructure has potential implications for oxide ion conductivity. We have therefore undertaken a thorough characterization of this material, including ionic conductivity measurements by impedance spectroscopy, detailed structural characterization by variable temperature powder X-ray and neutron diffraction, and computational simulations of oxide ion mobility by ab initio molecular dynamics methods.

---

*Corresponding author. E-mail: ivana.radosavljevic@durham.ac.uk.

(1) Goodenough, J. B. *Annu. Rev. Mater. Res.* **2003**, *33*, 91–128.
(2) Knauth, P.; Tuller, H. L. *J. Am. Ceram. Soc.* **2002**, *85*, 1654–1680.
(3) Mairesse, G. *C. R. Acad. Sci. Ser. C* **1999**, *2*, 651–660.
(4) Ramamoorthy, R.; Dutta, P. K.; Akbar, S. A. *J. Mater. Sci.* **2003**, *38*, 4271–4282.
(5) Ormerod, R. M. *Chem. Soc. Rev.* **2003**, *32*, 17–28.
(6) Steele, B. C. H. *J. Mater. Sci.* **2001**, *36*, 1053–1068.
(7) Harwig, H. A. *Z. Anorg. Allg. Chem.* **1978**, *444*, 151–166.
(8) Takahashi, T.; Iwahara, H. *Mater. Res. Bull.* **1978**, *13*, 1447–1453.
(9) Shuk, P.; Wiemhofer, H. D.; Guth, U.; Gopel, W.; Greenblatt, M. *Solid State Ionics* **1996**, *89*, 179–196.
(10) Michel, C.; Caignaert, V.; Raveau, B. *J. Solid State Chem.* **1991**, *90*, 296–301.

Experimental Section

Polycrystalline $Bi_8La_{10}O_{27}$ was made from a stoichiometric mixture of La_2O_3 (99.9%, Sigma-Aldrich) and Bi_2O_3 (99.995%, Alfa-Aesar) by solid state methods. Prior to weighing, the starting La_2O_3 oxide was fired at 900 °C to remove absorbed carbon oxide and water and Bi_2O_3 oxide was dried at 400 °C. The mixture was calcined at 700 °C for 12 h. After grinding, the calcined powder was uniaxially pressed into pellets. The pellets were fired at 1000 °C for 24 h, which led to pellets with ~60% theoretical density. Firing the pellets at higher temperature resulted in partial decomposition, although it increased the density by ~5−10%.

AC impedance spectroscopy measurements from 200 °C to 1000 °C in air were carried out with a Solartron 1260 frequency response analyzer over a frequency range of $10^{-2}-10^{6}$ Hz. The pellet was coated with platinum paste on each face, mounted in a ProboStat measurement cell and fired at 800 °C for 30 min to burn out the organic components in the paste to form platinum electrodes. Zview3.0a software was used to analyze the complex impedance data.

All laboratory powder X-ray diffraction data were collected on a Bruker AXS D8 Advance diffractometer with a Vantec detector, using Cu $K\alpha_1$ radiation, and an Anton Paar HTK1200 high-temperature attachment. Data were collected on heating and cooling every 20° between room temperature and 1000 °C, over a 2θ range of 10 to 90° in 0.017° steps with a data collection time of 0.5 s per step, resulting in an overall measurement time of 45 min per pattern. Neutron diffraction data were collected at room temperature and 750 °C on an 8.5 g sample on instrument D2B at Institut Laue Langevin, using a Ge (335) monochromator (λ = 1.594 Å) and an array of 64 ^{3}He detectors spaced at 2.5° intervals. Nine scans in 25 steps of 0.05° at 75 s per step were recorded and summed, resulting in total data collection time of 4.7 h at each temperature. Synchrotron X-ray data collections were performed at room temperature and 750 °C on the high-resolution powder diffraction beamline ID31 at the ESRF, using a wavelength of 0.3527 Å (determined from a Si standard). The polycrystalline sample was loaded into a 0.7 mm quartz capillary, which was rotated to promote random orientation of crystallites. Data were collected for 3 h at each temperature. All powder diffraction data were analyzed using Topas Academic software.[11]

Computational studies were performed by the ab initio molecular dynamics (AIMD) method to ensure accurate simulations, allowing bond breaking and formation due to the diffusion of oxygen ions. DFT-based first principle calculations were performed using the projector-augmented wave (PAW) formalism[12] of the Kohn-Sham DFT[13,14] at the generalized gradient approximation level (GGA), implemented in the Vienna ab initio simulation package (VASP).[15,16] The GGA was formulated by the Perdew−Burke−Ernzerhof (PBE)[17,18] density functional. The Gaussian broadening technique was adopted, and all results were well converged with respect to k-mesh and energy cutoff for the plane wave expansion. AIMD simulations were performed, following geometry optimization to reduce residual forces on atoms, in the NVT ensemble, temperature being controlled with a Nosé thermostat. MD simulations were run at four temperatures: 473 K, 773 K, 1073 K, and 1273 K. The MD time-step was 2 fs, and all simulations were run for 20 000 steps, allowing 40 ps to be reached. The highest temperature simulation was continued in the NVE ensemble to check that quantities extracted from the MD simulation were not affected by the thermostat. The MD simulations were analyzed visually using the LAMP program,[19] and mean-square-displacements to characterize the vibrational or diffusional motion were calculated with the nMoldyn code.[20]

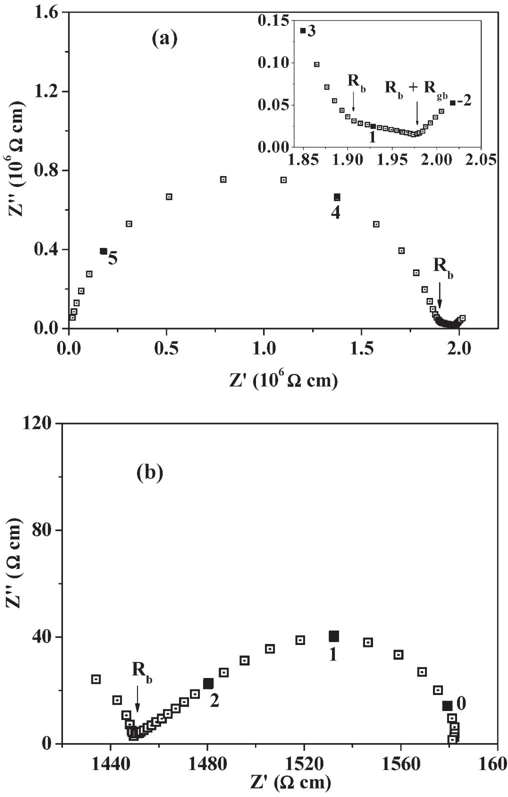

Figure 1. Complex impedance $Z''-Z'$ plots of $Bi_8La_{10}O_{27}$ at (a) 247 °C and (b) 560 °C. The inset in (a) shows an enlarged view of grain boundary and electrode responses in the low frequency range at 247 °C. The numbers denote the selected frequency logarithms in each plot. R_b and R_{gb} denote bulk and grain boundary resistivity, respectively.

Results and Discussion

Impedance Spectroscopy. At temperatures below 200−300 °C, the impedance data comprised bulk, grain boundary, and electrode responses. Figure 1a shows the complex impedance $Z''-Z'$ plot at 247 °C. The large semicircular arc was ascribed to bulk response, which can be modelled with a parallel resistor (R_b) and capacitor (C_b) elements.[21] The capacitance associated with the bulk response estimated from $\omega R_b C_b = 1$ ($\omega = 2\pi f_{max}$, f_{max} is the frequency at maximum imaginary impedance Z''_{max}, the intercept of the semicircular arc at low frequency was

---

(11) Coelho, A. A. Topas Academic, v 4.1, 2008.
(12) Blochl, P. E. *Phys. Rev. B* **1994**, *50*, 17953–17979.
(13) Hohenberg, P.; Kohn, W. *Phys. Rev. B* **1964**, *136*, B864–&.
(14) Kohn, W.; Sham, L. J. *Phys. Rev.* **1965**, *140*, 1133.
(15) Kresse, G.; Furthmuller, J. *Comput. Mater. Sci.* **1996**, *6*, 15–50.
(16) Kresse, G.; Joubert, D. *Phys. Rev. B* **1999**, *59*, 1758–1775.
(17) Perdew, J. P.; Burke, K.; Ernzerhof, M. *Phys. Rev. Lett.* **1996**, *77*, 3865–3868.
(18) Perdew, J. P.; Burke, K.; Ernzerhof, M. *Phys. Rev. Lett.* **1997**, *78*, 1396–1396.
(19) LAMP. The Large Array Manipulation Program. http://www.ill.eu/instruments-support/computing-for-science/cs-software/all-software/lamp (accessed June 19, 2009).
(20) Rog, T.; Murzyn, K.; Hinsen, K.; Kneller, G. R. *J. Comput. Chem.* **2003**, *24*, 657–667.
(21) Irvine, J. T. S.; Sinclair, D. C.; West, A. R. *Adv. Mater.* **1990**, *2*, 132–138.

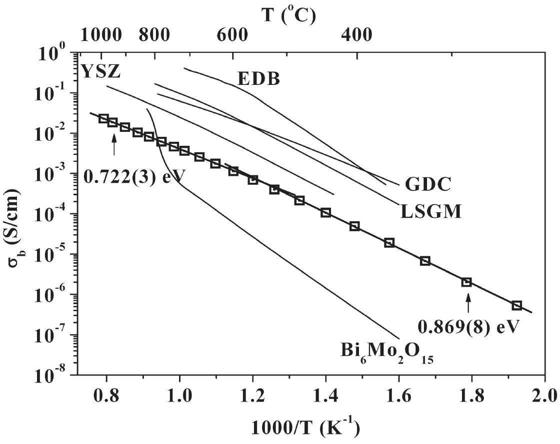

Figure 2. Arrhenius plot of bulk conductivity σ_b of $Bi_8La_{10}O_{27}$: a slight change of slope is observed between 500 and 600 °C; the activation energies in the low and high temperature regions are marked. Conductivity of some conventional oxide ion conductors, for example, $(ZrO_2)_{0.92}(Y_2O_3)_{0.08}$ (YSZ), $Bi_{0.8}Er_{0.2}O_{1.5}$ (EDB), GDC ($Ce_{0.9}Gd_{0.1}O_{1.95}$), and $La_{0.8}Sr_{0.2}Ga_{0.83}Mg_{0.17}O_{2.815}$ (LSGM) and of the recently reported fluorite-related bismuth-molybdates $Bi_{2n+4}Mo_nO_{6(n+1)}$, n = 3, 4, 5, 6 ($Bi_6Mo_2O_{15}$ is given as a representative), are plotted for comparison.

extracted as bulk resistivity R_b) is ~4 pF/cm. The small arc at the right hand of bulk response (enlarged in the inset of Figure 1a) is a grain boundary response, which showed a ~10^{-10} F/cm capacitance.[21] A Warburg electrode response was observed in the low frequency range 10^{-1}−10^{-2} Hz, which showed a capacitance ~10^{-8}−10^{-7} F/cm, indicative of ionic conduction response.[21,22] With increasing temperature, the bulk response gradually disappeared and the grain boundary and electrode responses dominated the impedance data. Figure 1b shows the complex impedance $Z''-Z'$ plot at 560 °C. The electrode response, which exhibited larger capacitances within 10^{-7}−10^{-6} F/cm at frequencies below 10 Hz, collapsed down to a semicircular arc, which overlapped with the grain boundary response to form a half-drop-tear-shaped (HDT) arc; the intercept at high frequency of the arc was estimated as bulk resistivity.

Figure 2 shows the Arrhenius plot of bulk conductivity. At 600 °C, $Bi_8La_{10}O_{27}$ showed conductivity of about 0.001 S/cm, and by 1000 °C it reached a magnitude of 0.02 S/cm. The grain and grain boundary response of $Bi_8La_{10}O_{27}$ could be well-resolved from the AC impedance data despite the low pellet density (60%). The grain boundary resistance is far smaller than the grain resistance, indicating that bulk conduction dominates in the pellet. Given the density of the pellet, however, the absolute conductivity values derived from AC impedance measurement cannot be taken as fully representative of the real bulk conductivity of the material; $Bi_8La_{10}O_{27}$ may display higher bulk conductivity if denser pellets were available. However, these could not be obtained without partial decomposition of the material.

A slight slope change on the Arrhenius plot was observed between 500 and 600 °C, and the activation energy decreased from 0.869(8) eV in the low temperature region between 200 and 500 °C to 0.722(3) eV in the high temperature region between 600 and 1000 °C. The change of activation energy could potentially be associated with a local oxide ion order−disorder transition at high temperature, where the oxide ions become increasingly mobile.

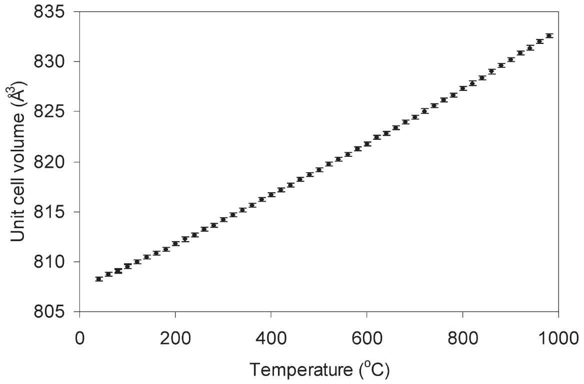

Figure 3. Variation of the unit cell volume of $Bi_8La_{10}O_{27}$ between room temperature and 1000 °C.

The oxide ion (bulk) conductivity of $Bi_8La_{10}O_{27}$ is lower than that for EDB ($Bi_{0.8}Er_{0.2}O_{1.5}$), YSZ $(ZrO_2)_{0.92}(Y_2O_3)_{0.08}$, GDC ($Ce_{0.9}Gd_{0.1}O_{1.95}$), and LSGM ($La_{0.8}Sr_{0.2}Ga_{0.83}Mg_{0.17}O_{2.815}$),[23−25] but it is higher than the conductivities of the recently reported family of fluorite-related bismuth-molybdates $Bi_{2n+4}Mo_nO_{6(n+1)}$, n = 3, 4, 5, 6, in the intermediate temperature range, up to 800 °C.[26,27]

Variable Temperature PXRD: Stability and Thermal Expansion of $Bi_8La_{10}O_{27}$. Variable temperature powder X-ray diffraction data were analyzed by the Rietveld method, using the structure published by Michel et al.[10] as a starting model. In these refinements the atomic fractional coordinates were kept fixed, and the refined parameters included unit cell dimensions, an overall isotropic temperature factor, scale factor, sample height, background, and peak shape function parameters. The temperature dependence of the $Bi_8La_{10}O_{27}$ unit cell volume is shown in Figure 3. It exhibits a smooth variation, suggesting an absence of structural phase transitions in this temperature range. The volume thermal expansion coefficient calculated for this temperature range is $\alpha_V = 3.34(5) \times 10^{-5}\ K^{-1}$.

The in situ variable temperature PXRD experiments demonstrated that pure $Bi_8La_{10}O_{27}$ is stable as a single phase up to 1000 °C. On further heating above 1050 °C it undergoes decomposition into a mixture of La_2O_3 and $BiLa_2O_{4.5}$, accompanied by a loss of Bi_2O_3.

Variable Temperature Powder Synchrotron and Neutron Diffraction. To improve the existing room temperature

---

(22) Macdonald, J. R. *Impedance Spectroscopy: Emphasizing Solid State Materials and Systems*; Wiley: New York, 1987.

(23) Kharton, V. V.; Marques, F. M. B.; Atkinson, A. *Solid State Ionics* **2004**, *174*, 135–149.

(24) Huang, K. Q.; Feng, M.; Goodenough, J. B. *J. Am. Ceram. Soc.* **1998**, *81*, 357–362.

(25) Huang, K. Q.; Tichy, R. S.; Goodenough, J. B. *J. Am. Ceram. Soc.* **1998**, *81*, 2565–2575.

(26) Vila, E.; Rojo, J. M.; Iglesias, J. E.; Castro, A. *Chem. Mater.* **2004**, *16*, 1732–1739.

(27) Vila, E.; Landa-Canovas, A. R.; Galy, J.; Iglesias, J. E.; Castro, A. *J. Solid State Chem.* **2007**, *180*, 661–669.

structural model and to investigate the high temperature structure, we used a combination of simulated annealing and Rietveld refinement applied simultaneously to powder synchrotron X-ray and neutron diffraction data. This data analysis approach has proved reliable and successful in determining the crystal structures of very complex oxide materials from high quality powder diffraction data, including the 176-atom pyrochlore-type superstructure α-$Bi_2Sn_2O_7$ and 136-atom ZrP_2O_7 and HfP_2O_7.[28,29]

Inspection of unit cell parameters of $Bi_8La_{10}O_{27}$ suggested a relationship between this phase and the fluorite-type δ-Bi_2O_3. The starting structural model for our data analysis was therefore obtained by transforming the δ-Bi_2O_3 structure using the following matrix:

$$\begin{bmatrix} 3/2 & 0 & 3/2 \\ 0 & 3 & 0 \\ -1/2 & 0 & 1/2 \end{bmatrix}$$

In space group *Immm*, this led to an asymmetric unit containing a total of four metal sites and six possible oxygen sites. The cation distribution was derived from refinements in which all four metal sites were populated by Bi and their fractional coordinates and isotropic temperature factors were refined against synchrotron X-ray diffraction data. Atoms on Wyckoff sites 8n and 2a ended up with significantly higher b_{iso} values than those on positions 4e and 4g, suggesting that they were occupied by lighter La cations. This assignment features La, rather than lone-pair containing Bi(III), on the inversion center, and it confirms the metal ordering scheme reported by Michel et al.[10]

All subsequent structure analysis was performed on combined synchrotron and neutron diffraction data sets. For a fluorite-derived structure there are six possible oxygen sites, and the distribution of oxygen atoms over these sites was investigated using a model in which their occupancies were refined while the isotropic temperature factors were kept equal and fixed (at b_{iso} = 1.5 Å^2). A restraint which kept the overall oxygen content at 27 per chemical formula unit, without imposing any specific restraints on occupancies on individual sites, was used. Temperature factors were kept fixed during this process. Fractional occupancies of four oxygen sites refined to values between 0.95 and 1.05, and these were considered to be fully occupied in all further analyses. This led to a final structural model in which all atomic fractional coordinates were refined, along with anisotropic atomic displacement parameters for all metals and for the four fully occupied oxygen sites; fractional occupancies for O(5) and O(6) were also refined (with the restraint described earlier), along with an equated isotropic temperature factor for the two sites.

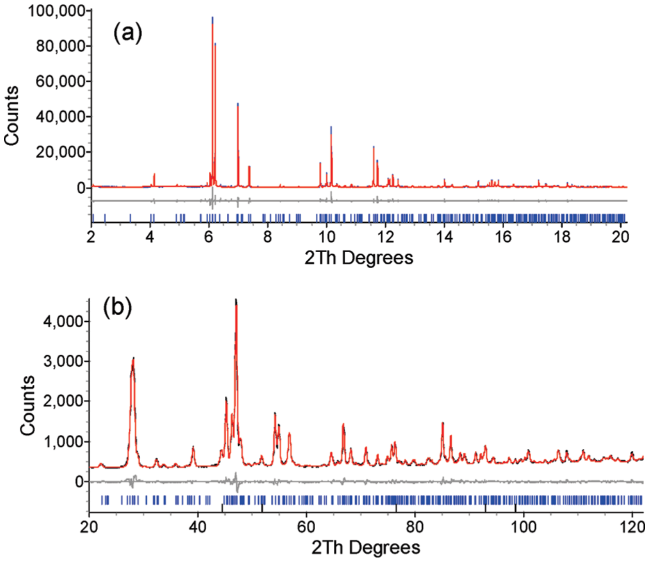

Figure 4. Rietveld plots for $Bi_8La_{10}O_{27}$ room temperature data: (a) synchrotron X-ray diffraction; (b) neutron diffraction. A small number of weak extra peaks present in the neutron pattern are due to an F-centred cubic phase, identified as the Rh−Pt thermocouple used in the experimental setup; these were fitted as a second phase in the Rietveld refinement.

Table 1. Structural Parameters for $Bi_8La_{10}O_{27}$ at Room Temperature: *a* = 12.0640(3) Å, *b* = 16.3564(4) Å, *c* = 4.09871(6) Å, and *V* = 808.77(4) Å^3

atom[a]	site	*x*	*y*	*z*	occ	U_{eq} (Å^2)
Bi1	4e	0.3110(1)	0	0	1	0.009
Bi2	4g	0	0.3310(1)	0	1	0.010
La1	8n	0.3417(2)	0.3257(1)	0	1	0.013
La2	2a	0	0	0	1	0.018
O1	4h	0	0.0888(5)	0.5	1	0.005
O2	4h	0	0.2759(3)	0.5	1	0.016
O3	8n	0.1894(5)	0.0879(3)	0	1	0.024
O4	8n	0.1523(3)	0.2638(3)	0	1	0.010
O5	8n	0.186(1)	0.458(1)	0	0.349(5)	0.036(2)[b]
O6	4h	0	0.32(1)	0.5	0.08(1)	0.036(2)[b]

[a] The numbering scheme used here lists oxygen atoms sequentially and in order of decreasing fractional occupancy; we note that this differs from the numbering used originally by Michel et al. [b] Refined as equated isotropic thermal displacement parameters.

The final agreement factors obtained were as follows: overall R_{wp} = 7.47%, R_{Bragg} (X-ray) = 1.72%, and R_{Bragg} (neutron) = 1.08%. The Rietveld plots of the room temperature data are shown in Figure 4, and details of the room temperature structural model are given in Table 1.

The structure obtained at room temperature was used as a starting model for high temperature diffraction data analysis, using the same refinement strategy. The final agreement factors obtained were as follows: overall R_{wp} = 7.22%, R_{Bragg} (X-ray) = 2.01%, and R_{Bragg} (neutron) = 0.91%. The Rietveld plots of the 750 °C data are shown in Figure 5, and the structural details are in Table 2.

Structural models obtained for both room temperature and 750 °C suggest a very low, but non-zero, occupancy of site O(6). This site (Wyckoff site 4h, located in the channels) was not occupied in the final model reported by Michel et al.; instead, they proposed an oxygen sublattice

---

(28) Evans, I. R.; Howard, J. A. K.; Evans, J. S. O. *J. Mater. Chem.* **2003**, *13*, 2098–2103.
(29) Stinton, G. W.; Hampson, M. R.; Evans, J. S. O. *Inorg. Chem.* **2006**, *45*, 4352–4358.

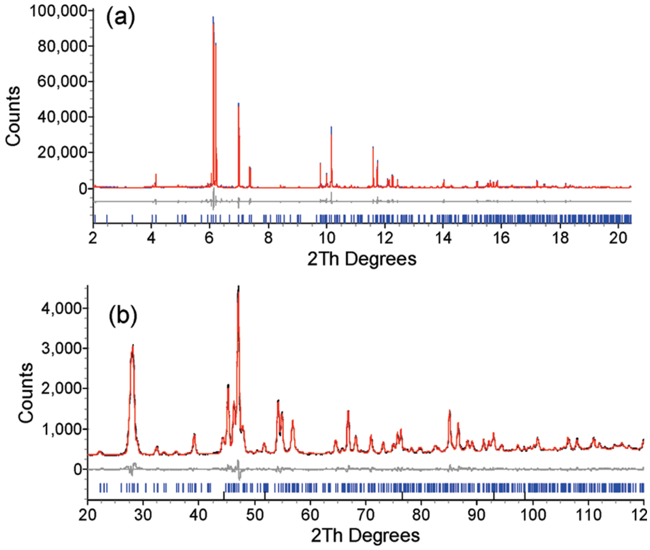

Figure 5. Rietveld plots for $Bi_8La_{10}O_{27}$ 750 °C data: (a) synchrotron X-ray diffraction; (b) neutron diffraction. A small number of weak extra peaks present in the neutron pattern are due to an F-centred cubic phase, identified as Rh−Pt thermocouple used in the experimental setup; these were fitted as a second phase in the Rietveld refinement.

Table 2. Structural Parameters for $Bi_8La_{10}O_{27}$ at 750 °C: *a* = 12.1372(3) Å, *b* = 16.4738(3) Å, *c* = 4.13539(7) Å, and *V* = 826.86(3) Å^3

atom[a]	site	*x*	*y*	*z*	occ	U_{eq} (Å^2)
Bi1	4e	0.3132(2)	0	0	1	0.038
Bi2	4g	0	0.3315(2)	0	1	0.028
La1	8n	0.3406(2)	0.3271(2)	0	1	0.021
La2	2a	0	0	0	1	0.042
O1	4h	0	0.0911(9)	0.5	1	0.006
O2	4h	0	0.2764(7)	0.5	1	0.052
O3	8n	0.1884(8)	0.0902(6)	0	1	0.075
O4	8n	0.1512(4)	0.2634(4)	0	1	0.033
O5	8n	0.191(2)	0.464(1)	0	0.358(5)	0.068(4)[b]
O6	4h	0	0.34(3)	0.5	0.05(1)	0.068(4)[b]

[a] The numbering scheme used here lists oxygen atoms sequentially and in order of decreasing fractional occupancy; we note that this differs from the numbering used originally by Michel et al. [b] Refined as equated isotropic thermal displacement parameters.

which, in addition to the four fully occupied crystallographic positions, had the remaining oxygen atoms on the O(5) site. Interestingly, their refinement against the neutron diffraction data suggested a fractional occupancy of 0.34 for this site, but this was fixed at 0.375, to comply with the $Bi_8La_{10}O_{27}$ formula.[10] We deemed it relevant to reconsider the occupancy of O(6), even at very low levels, because of the potential role of this fluorite-derived crystallographic site in the oxide ion migration pathway (vide infra).

Description of Structure and Possible Pathways for Oxide Ion Migration. The room temperature crystal structure of $Bi_8La_{10}O_{27}$, the ordering pattern of Bi^{3+} and La^{3+} cations, and their coordination environments have been described before,[10] and we therefore focus only on those structural features which can be associated with oxide ion conduction that we have observed in this material. A polyhedral representation of the $Bi_8La_{10}O_{27}$ structure is shown in Figure 6. The structure can be described as consisting of a framework of edge-sharing OM_4 (M = Bi, La) tetrahedra, similar to those found in δ-Bi_2O_3, arranged in a way that gives rise to channels running along the *c* crystallographic axis, located at (0, 1/2, *z*), (1/2, 0, *z*), (1/2, 1, *z*), and (1, 1/2, *z*). It is in these channels that the Bi(III) lone-pairs are presumably located, as well as the chains formed by the Bi(1) atoms bonded to oxygen atoms disordered over partially occupied O(5) sites, which display large anisotropic atomic displacement parameters (Figure 6).

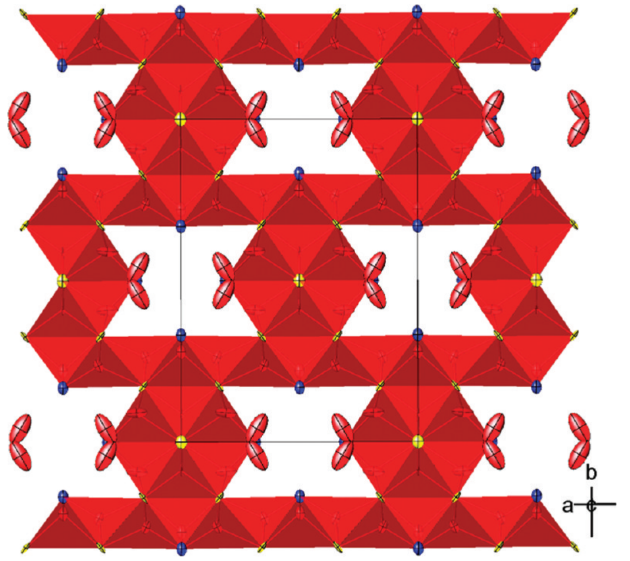

Figure 6. Polyhedral representation of the $Bi_8La_{10}O_{27}$ structure: Bi atoms are shown in blue, La in yellow, O atoms in red; red tetrahedra represent OM_4 (M = Bi, La) groups. Large anisotropic atomic displacement parameters are found for the disordered partially occupied site O(5).

These partially occupied sites located in channels along the *c*-axis presumably have an important role in facilitating oxide ion conductivity in $Bi_8La_{10}O_{27}$. Each O(5) oxygen atom is bonded to two Bi atoms at 2.18 Å. The nearest oxygen atoms are two O(3) sites at 2.72 Å, two O(6) positions at 3.09 Å, and an O(4) site at 3.24 Å. Two mutually perpendicular views of this arrangement are depicted in Figure 7. They suggest that possible conduction mechanisms through the channels can involve thermally induced hopping of oxide ions between the partially occupied disordered O(5) positions via O(3) sites, via O(6) positions, or by a combination of the two. From the standpoint of crystallochemistry, the occupation of the O(6) site in this structure is plausible. If located on this site, an oxygen atom would be in a tetrahedral coordination environment, bonded to two Bi(1) cations in the channels at about 2.50 Å and two Bi(2) atoms belonging to the fluorite-like OM_4 framework at about 2.65 Å.

Computational Modelling and Proposed Pathway for Oxide Ion Migration. AIMD simulations were performed to probe the possible conduction pathways suggested by diffraction-based crystallographic analysis. The structural model for all simulations, which cannot include fractionally occupied sites, was constructed from the crystallographic model by (i) doubling the cell in the *c*-direction, (ii) removing half of the O(5) sites in the form of rows of oxide ions, and (iii) from the remaining O(5)

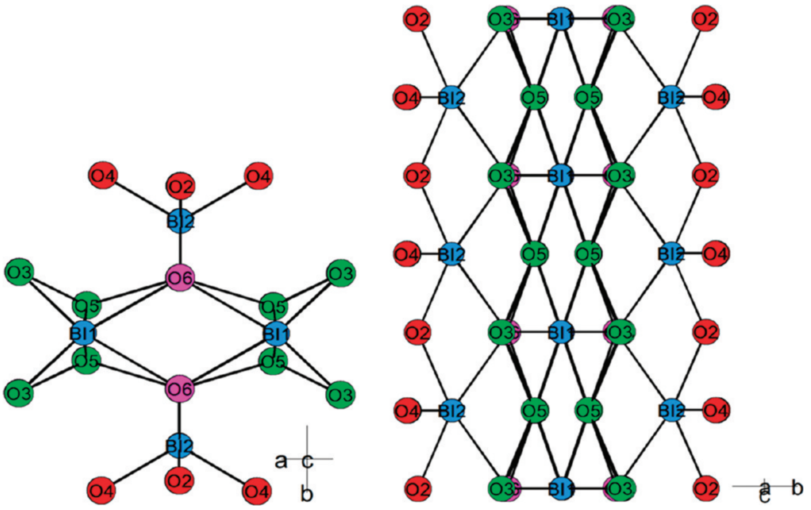

Figure 7. Schematic representation of crystallographic sites in channels along the *c*-axis in the $Bi_8La_{10}O_{27}$ structure, drawn in the (*ab*) and in the (*bc*) plane. Bi atoms are shown in blue, O(3) and O(5) sites in green, and the vacant O(6) site in pink; oxygen atoms sites which do not form part of plausible pathways along the channels are drawn in red.

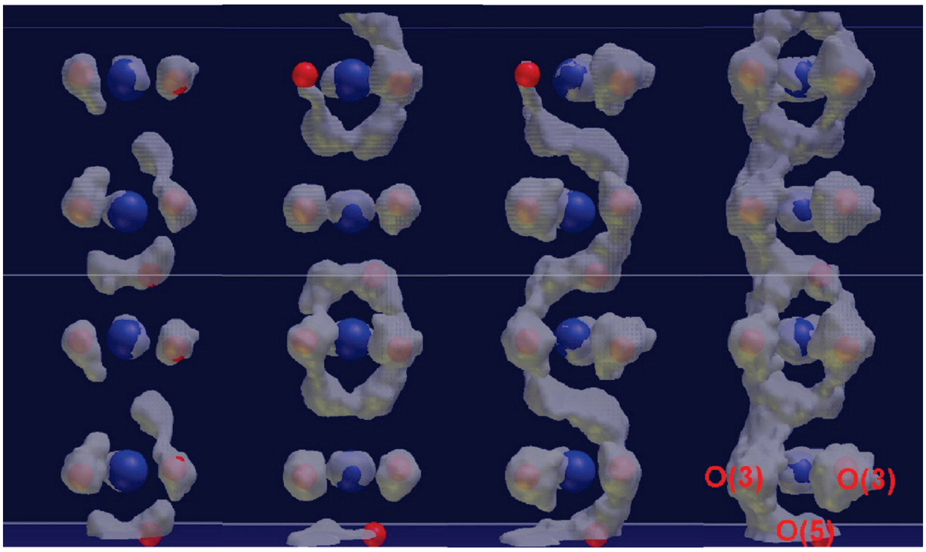

Figure 8. Channel at (0, 1/2, *z*), shown in the same view as Figure 7b: white clouds represent volume visited by ions during MD simulations at (left to right) 473 K, 773 K, 1073 K, and 1273 K; Bi atoms shown in blue, O in red.

sites, removing one oxygen atom in each channel. In this way, the model contained 90 atoms (16 Bi, 20 La, and 54 O), matching the known stoichiometry, and two channels, each one including three out of four initially populated O(5) crystallographic sites.

Figure 8 shows as white clouds the volume visited by each oxygen and bismuth ion as a function of temperature for the channel centered at (x = 0, y = 1/2, z). The simulation cell has been doubled in the *c*-direction for visualization. Only the two Bi ions and the five oxide ions on the side of the channel including the O(5) vacancy defect are considered. With increasing temperature, it is clear that the Bi ions are almost fixed in position whereas the oxide ions progressively visit more volume, and volumes being visited by neighbouring oxide ions become connected. At the two highest temperatures, the white clouds of occupied volume form continuous channels in the *c*-direction.

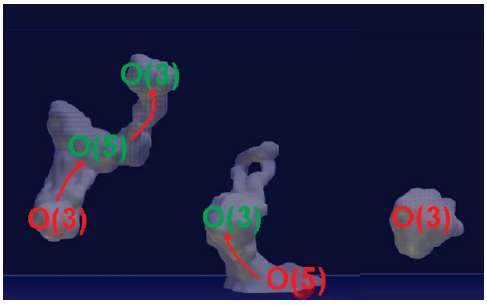

Figure 9. Volumes visited by three individual oxide ions in the channel at (0, 1/2, *z*).

Whether the motion of the oxide ions remains vibrational or becomes diffusional at higher temperature can be investigated in two ways. Firstly, the cloud plots of Figure 8 can be decomposed into individual oxide ion contributions. This information is shown in

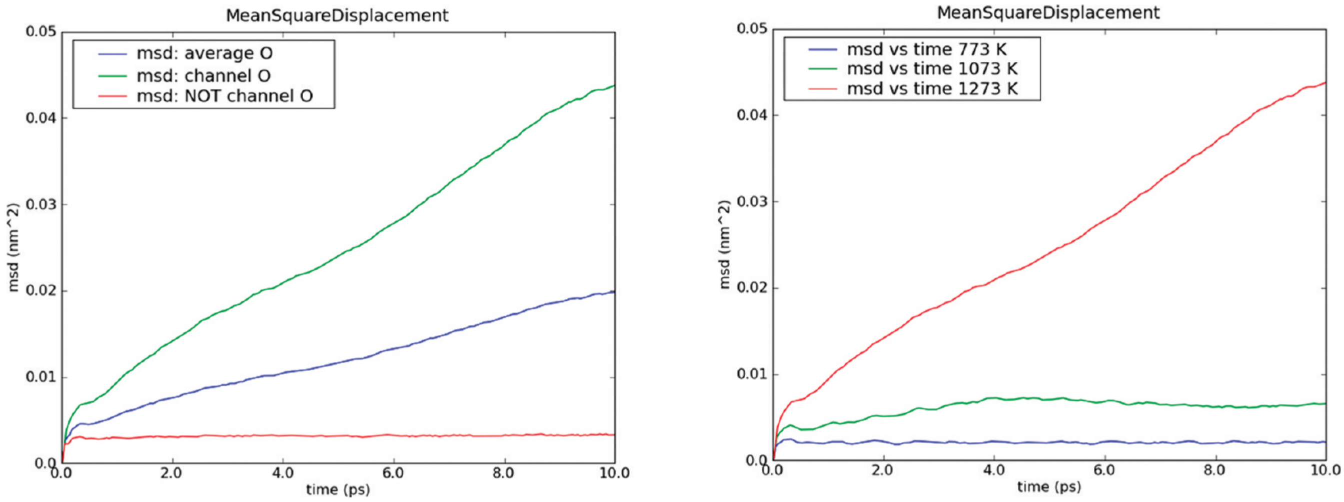

Figure 10. Mean square displacements (MSD) of different groups of atoms: (a) mobility of O(3) and O(5) oxide ions in channels (green curve) is double the average mobility of oxygen (blue curve). All other O sites give an MSD characteristic of non-mobile oxygen (red curve); (b) MSD of O(3) and O(5) oxygens as a function of temperature shows that at 773 K and 1073 K the oxygen ions explore fixed volumes (blue and green curves), whereas diffusion is present at 1273 K (red curve).

Figure 9 for three oxide ions in the channel (highlighted in Figure 8). A range of dynamics can be seen. One oxygen atom on an O(3) site (right) remains localized, vibrating about its equilibrium position, whereas another O(3) oxygen (left) moves about 4 Å and visits an O(5) site and a second O(3) site. The remaining oxide ions in this channel also travel several angstroms, and similar behavior is seen for the other channel in the model.

Oxide ion motion can be quantified by calculating the mean-square-displacement (MSD) of different groups of atoms. Figure 10a shows the average MSD for all oxide ions, the MSD for oxide ions on O(3) and O(5) sites in the channels, and the MSD for all other oxide ions. The linearly increasing MSD of the O(3) and O(5) ions indicates diffusional motion, whereas the small, constant MSD for the other oxygens is characteristic of strongly localized ions. The diffusion of the channel oxide ions can also be analyzed as a function of temperature, Figure 10b. At 773 K and 1073 K, the motion is vibrational, with progressively bigger volumes of space being explored, while diffusion only sets in on the ~10 ps time scale at 1273 K.

One further issue concerns the extent to which ion motions are concerted or correlated. This is addressed by considering the time dependence of the coordinates of the oxide ions on the O(3) and O(5) sites, Figure 11. The Cartesian coordinates for the O(5) and O(3) ions are shown for the last 20 ps of the 1273 K MD trajectory, with steps indicating significant, rapid changes in oxide ion positions. The oxide ion labelled O3_1 corresponds to the bottom right plot of Figure 9, and its time-dependent coordinate variation is purely vibrational. All other ions exhibit jumps. The vertical dashed lines indicate the extent to which ionic motion is correlated, for example ions O3_2 and O3_3 jump simultaneously at 29 ps and then back at 32 ps which coincides with a jump of the O3_4 O ion. Ions can only move significant distances when free space exists, and in this situation the ions move rapidly over several hundred femtoseconds to their new positions.

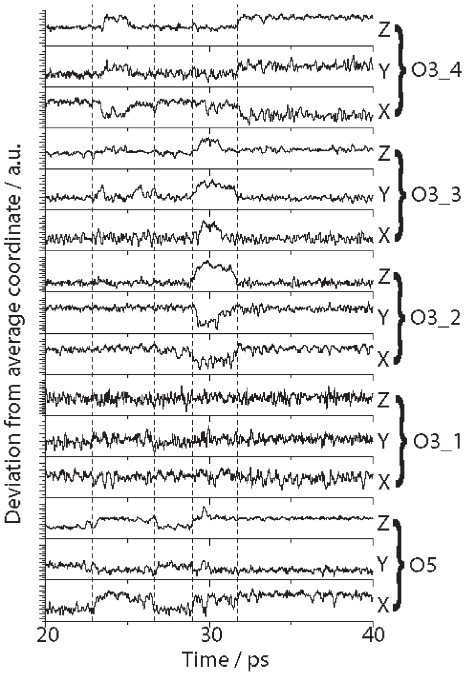

Figure 11. Coordinates of five atoms in the channel at (0, 1/2, z) obtained for the 1273 K MD simulation; dashed lines show that jumps of different oxide ions in the channel are concerted.

The role of the partially occupied O(5) and the O(6) sites in facilitating oxide ion diffusion is also revealed by these MD simulations. In the (0, 1/2, z) channel in the simulation model, there is a fully occupied side and a side in which only one of two O(5) sites is initially occupied. Only the channel side with the vacant O(5) site (defect) shows diffusion. However, the situation for the channel at (1/2, 0, z) is different since an O(5) oxide ion migrates across the channel, giving rise to diffusion on both sides of the channel. This is manifested as the continuity in the cloud plots between the O(5) sites on the two sides of the channel, shown in the (*ab*) plane projection in Figure 12.

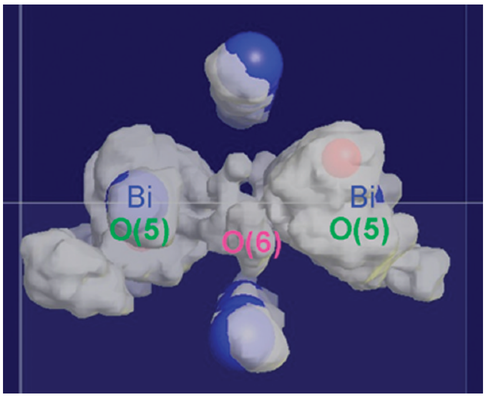

Figure 12. Oxide ion mobility across the channel at (1/2, 0, *z*) viewed as the (*ab*) plane projection (for comparison with the view of the structure shown in Figure 7a).

The cross-channel diffusion appears to occur via the O(6) sites. Although these sites appear essentially unoccupied in the average picture obtained from the diffraction data (Tables 1 and 2), Figure 12 shows that they are indeed visited in the duration of the MD simulations.

Conclusions

Fluorite-related bismuth lanthanum oxide $Bi_8La_{10}O_{27}$ exhibits oxide ion conductivity of 2×10^{-2} S/cm at 1000 °C. It is stable up to this temperature, but above 1050 °C it decomposes into a mixture of La_2O_3 and $BiLa_2O_{4.5}$. $Bi_8La_{10}O_{27}$ does not undergo any clear crystallographic phase transitions in the temperature range studied, and the decrease of the activation energy from 0.869(8) eV below 600 °C to 0.722(3) eV above this temperature is presumably associated with local disordering of oxide ions, leading to their increased mobility. Our synchrotron X-ray and neutron powder diffraction based structural analysis offers insight into possible conduction pathways along the channels down the *c*-axis. Ab initio molecular dynamics simulations identify the crystallographic sites involved in the conduction process. Concerted oxide ion hopping occurs among the O(3) sites and the disordered partially occupied O(5) sites along the channels, aided by cross-channel migration via the vacant tetrahedrally “coordinated” interstitial O(6) sites. The combination of experimental and computational studies provides a coherent picture of the structure−property relationships in this material.

Acknowledgment. IRE thanks the EPSRC for funding though Grant EP/F030371 and RCUK for an Academic Fellowship. Irene Margiolaki (ESRF), Emmanuelle Suard (ILL), and Sarah Lister and John Evans (Durham University) are acknowledged for their assistance with synchrotron X-ray and neutron data collections.